



# Mesoscopic damage evolution characteristics of sandstone with original defects based on micro-ct image and fractal theory

Yujun Zuo<sup>1,2</sup> · Zhibin Hao<sup>1</sup> · Hao Liu<sup>2,3</sup> · Chao Pan<sup>1</sup> · Jianyun Lin<sup>2</sup> · Zehua Zhu<sup>1</sup> · Wenjibin Sun<sup>1</sup> · Ziqi Liu<sup>1</sup>

Received: 21 February 2022 / Accepted: 2 October 2022 / Published online: 9 November 2022  
© Saudi Society for Geosciences 2022

## Abstract

To research the influence of different confining pressures on the damage evolution of defective sandstone, the sandstone numerical model with real mesostructure is established by RFPA<sup>3D</sup> using CT scan, and then carried out a triaxial compression test. The two-dimensional and three-dimensional mesoscale fracture box dimension algorithm using the digital image is compiled by MATLAB to quantitatively analyze the fractal characteristics. According to the research, as confining pressure increases, the stress corresponding to each characteristic point increases noticeably, and the specimen follows the law of transition from brittle to plastic failure under high confining pressure. The 0 MPa specimen is a tensile failure, the 5 MPa specimen is a tensile-shear mixed failure, and the 10 MPa and 15 MPa specimens are shear failures. Two types of fractal dimensions assess sandstone damage based on fracture development and fragmentation. The greater the fractal dimension, the more complete the fracture mode, and the greater the damage degree. Compared with other specimens, the mechanical characteristics and damage evolution of 0 MPa specimens are greatly different, and the fractal dimension is the largest.

**Keywords** Sandstone with original defects · Fracture mechanical properties · Fractal dimension · Confining pressure · Three-dimensional reconstruction

## Introduction

The interior of ore rock, as a heterogeneous natural geological material, is primarily composed of rock matrix, original defects, and other minerals. The random distribution of original defects in rock mass leads to a discontinuous, non-uniform, and anisotropy response, which affects not only the mechanical characteristics but also the fracture process and

mode. Comparing the crack distribution of specimens before and after loading deformation under confining pressures can simulate the different depths undermining conditions (Yang et al. 2008, 2012; Masri et al. 2014; Singh et al. 2015).

The fractal theory was founded by Mandelbrot (Mandelbrot 1998), and its research object is disordered and self-similar systems widely existing in nature and society (Wu 2017). Xie (1996) used fractal theory in the rock engineering field and found the theory of fractal rock mechanics. Through a high-speed camera (Chen et al. 2013), scanning

Responsible Editor: Murat Karakus

✉ Yujun Zuo  
Zuo\_yujun@163.com

Zhibin Hao  
haozhibin0712@163.com

Hao Liu  
liuhao\_gzu@163.com

Chao Pan  
cpan@gzu.edu.cn

Jianyun Lin  
jianyun0\_lin@163.com

Zehua Zhu  
zhuzehua202103@163.com

Wenjibin Sun  
sunwenjibin@163.com

Ziqi Liu  
liuziqi\_gzu@163.com

<sup>1</sup> Mining College, Guizhou University, Guiyang 550025, China

<sup>2</sup> School of Resource and Environmental Engineering, Guizhou University, Guiyang 550025, China

<sup>3</sup> Department of Civil and Environmental Engineering, Technical University of Catalonia, 08034 Barcelona, Spain

electron microscope (Yi and Zhao 1990; Mao et al. 2005), CT (Cnudde et al. 2006), and other technical equipment, the structural images of the surface and internal defects of the specimen can be obtained, and the relevant parameters of cracks can be extracted and the influence of internal defect distribution to rock material studied. Among them, CT, as a usual and trusty technique, can describe the internal structural characteristics and fracture damage. It provides a feasible method of the accurate establishment of a 3D numerical model (Hou et al. 2016). Some scholars established numerical models reflecting the real structure through the reconstruction of rock mesostructure and carried out related numerical simulation research (Yue 2006, Zhao et al. 2015, and Wang et al. 2016). Wu et al. (2016), Song et al. (2020), Wu et al. (2020), Liu et al. (2021), Tang et al. (2021), and Liu et al. (2022) took the two-dimensional fractal dimension of acoustic emission in the pre-peak stage as the characteristic parameter to quantitatively characterize the damage degree and spatial distribution characteristics of rock materials provides other means for studying the evolution law of mesoscopic scale fracture.

The existing research results are of the great significance of understanding the mechanical characteristics and rupture mechanism of defective rock mass, but they are mainly in view of the mechanical characteristics of rock fracture caused by simple internal structure, ignoring the meso-mechanical properties and real mesostructure, so it is hard to reflect the rupture mechanism of the ore rock. So, this paper takes the sandstone of the Jinfeng Gold Mine in Guizhou of China as the research object. The real-time mechanical characteristics and fracture characteristics of the heterogeneous real meso-sandstone mechanical model are simulated by RFPA<sup>3D</sup>. The damage evolution law of sandstone is analyzed from the aspects of stress–strain curve, stress evolution of characteristic strength point, crack propagation deformation law, and fracture process. The fractal dimension algorithm of the rock mesoscopic scale fracture box using MATLAB based on digital images is compiled to quantitatively characterize the degree of injury, analyzing dynamic development process of the internal crack in rock mass under confining pressure. It contributes to elucidating the fracture failure mechanism of rock mass and providing a research foundation for evaluating the engineering stability of rock mass.

## Specimens and methods

### Specimen collection and processing

The sandstone samples come from the Jinfeng Gold Mine of China, with a density of 2.70 g/cm, uniform texture, and good overall integrity. The mineralized areas and surrounding rocks near the mine in the study area are mainly

sandstone and clay rocks which form a rhythmic interbedding phenomenon with uneven thickness. The ore bodies are layered and plate-shaped. The  $Q$  value of the ore bodies is generally between 0.1 and 10, and the Platts coefficient  $f=2$  to 5 (Chen et al. 2022). With the continuous development of pioneering projects and mining operations to the deep, the engineering geology and the occurrence conditions of ore bodies are becoming more and more complicated, the geological structure is developed, the weathering is strong, the stability is poor, the joints and faults are developed, and some joints are open.

## Test method

### CT scan experiment and numerical image characterization

The digital image processing technique uses CT scanning to transform the research object into a digital image. The geometry and spatial distribution of meso-components are distinguished by grayscale and color, and the distribution of each medium is divided based on the segmentation threshold, thus obtaining the non-uniformity characterization image of materials (Hao et al. 2022).

This scanning test equipment adopts the X-ray 3D microscope nanoVoxel-4000 system as shown in Fig. 1a. CT scanning is mainly on account of the interaction of radiation with matter. As the ray passes through objects, a considerable portion of incident photons is scattered by matter (Wang et al. 2020; Wu et al. 2021), thereby weakening the intensity of the ray, and then converting it into a CT image by imaging technology (Fig. 1b). The scanned slice of Fig. 1c is obtained after scanning the schematic diagram of the specimen. The image resolution is 500 pixels  $\times$  500 pixels, and the full size is 50 mm  $\times$  50 mm. Different gray values represent different types of rock media. The lighter areas are high-density areas and mainly composed of calcite, while the black areas are low-density areas and mainly composed of holes and fissures in the rock, in which the gray areas are sandstone matrix parts whose density is between the former two (Wang et al. 2019). Import Fig. 1d into ImageJ and accurately divide the gray values of each pixel in the image to obtain the three-dimensional spatial distribution of gray values in Fig. 1e. The gray values of the three components are quite different, the area where the filling material is located is convex, and the color brightness is higher than that of sandstone matrix and original fracture. The threshold values of binarization are determined to be 100 and 140. Figure 1f is a digital representation image of the heterogeneity of sandstone mesostructure after digital image processing. Sandstone matrix, joints (calcite), and cracks are represented by green, pink, and blue, respectively, from which the spatial distribution and particle shape of main mineral components can be more clearly observed. This study uses

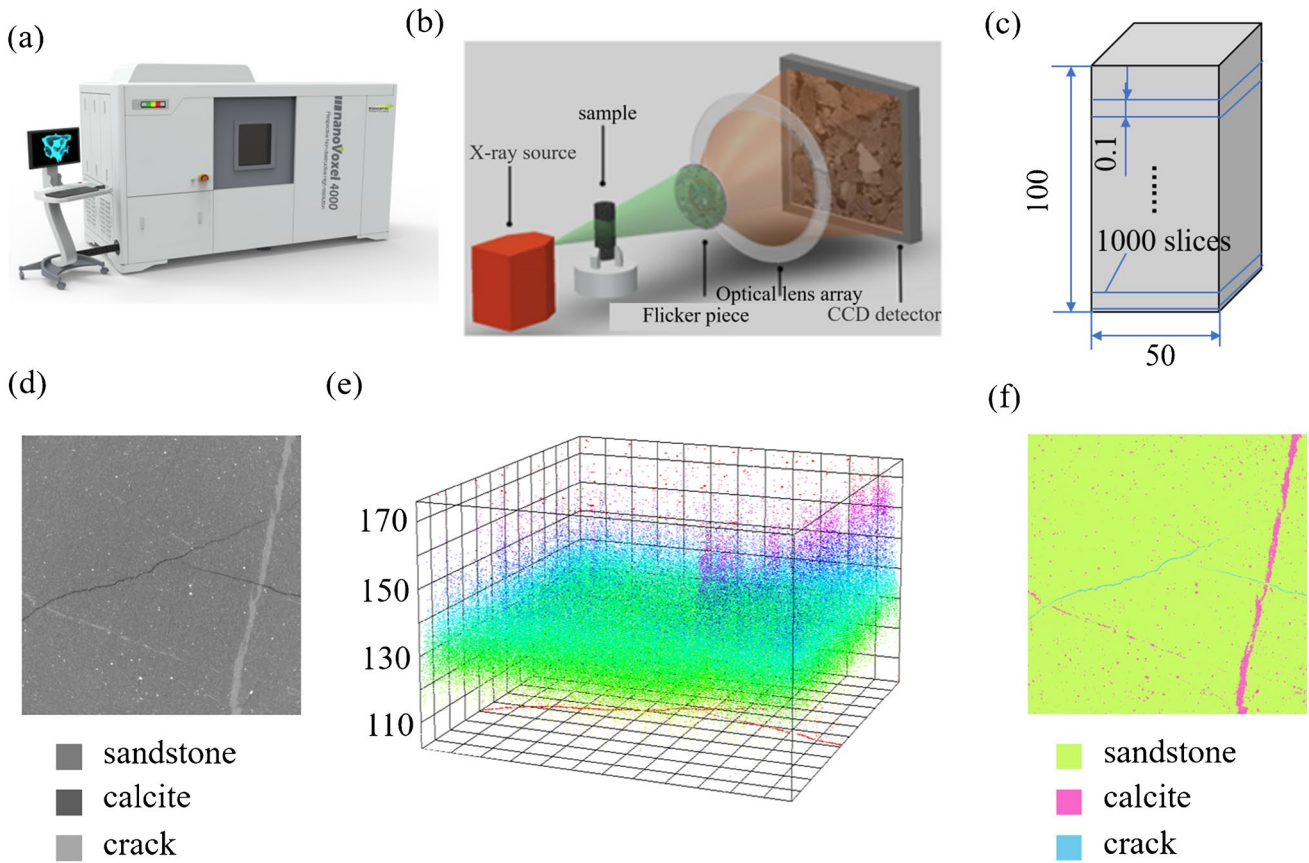


**Fig. 1** CT scan and digital image characterization process. **a** X-ray 3D microscope nanoVoxel-4000 system; **b** CT schematic diagram; **c** numerical model; **d** Two-dimensional CT slice; **e** Threshold segmentation graph; **f** Threshold-segmentation characterization image of sandstone

high-resolution CT scan images for modeling to better identify the color features at the intersection of different material types, so that we can more accurately identify it in the process of digital image characterization and carry out material area division and parameter assignment.

**Establishment of numerical model**

After the scanned pictures are numbered in sequence, they are converted into the form of model data, and then stacked and imported into RFPA<sup>3D</sup> along the Z-axis (Fig. 2a) to

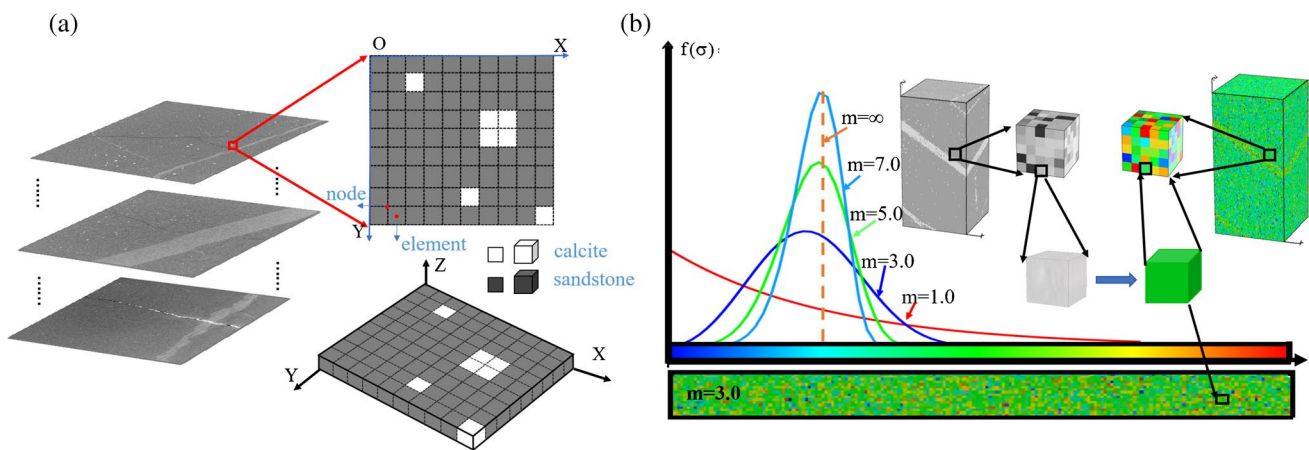


**Fig. 2** Numerical model building process: **a** image stack vectorization process; **b** parameter assignment process

**Table 1** Mechanical parameters of sandstone numerical model

Material	Elastic modulus/ GPa	Com- pressive strength/ MPa	Poisson ratio	Com- pression- tension ratio	Internal friction angle/ °
Sandstone	108.2	118	0.16	14	35
Calcite	80.5	101	0.30	11	30

complete the 3D structural model reconstruction. The volume pixel is regarded as a cube unit of the finite unit, and the image can be changed into many finite element cubes to characterize different mesoscopic materials in the sandstone specimen. Considering the non-uniformity of materials, this paper assumes that the mechanical properties of meso-elements follow the Weibull distribution, and its expression is

$$f(u) = \frac{m}{u_0} \left(\frac{u}{u_0}\right)^{m-1} \exp\left(-\frac{u}{u_0}\right)^m \quad (1)$$

Among them,  $u$  is the properties of the meso-elements;  $u_0$  is the mean value of properties of the meso-elements;  $m$  is the homogeneity of material, and the data generated with the increase of  $m$  is as shown in Fig. 2b. The non-uniform fluctuation characteristics of petrophysical properties can be mirrored in the meso-level through statistical function (Weibull 1951).

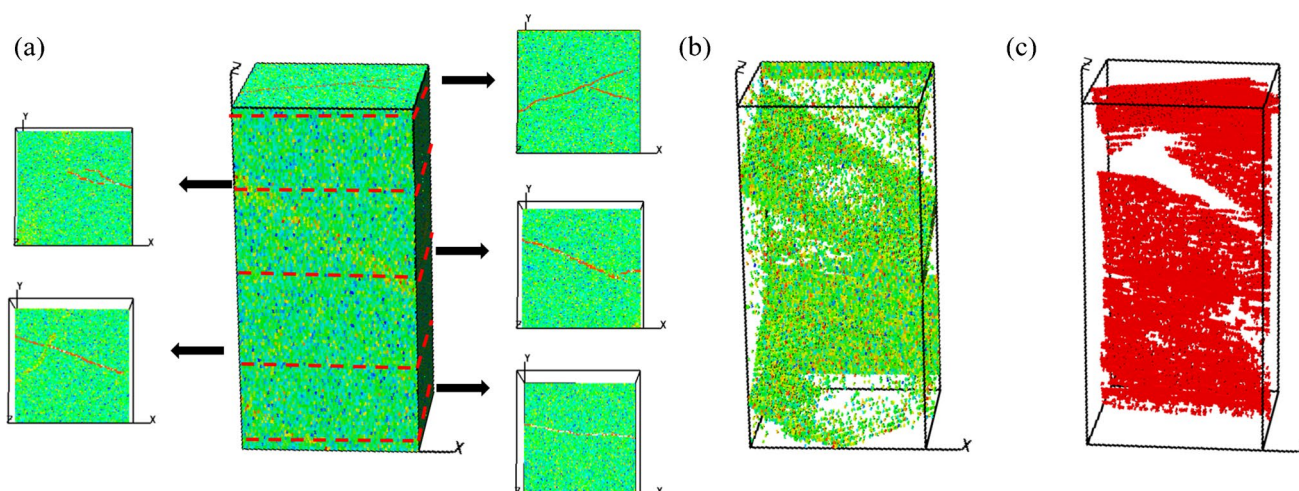
According to different colors, the material components are assigned values by the Monte-Carlo method based on the mechanical parameters shown in Table 1 and input the non-uniformity coefficient of them. The numerical model considering the real mesostructure of materials is shown in Fig. 3. Each specimen is based on digital image processing to ensure the same meso-medium. The specimen size is 50 mm × 50 mm × 100 mm, and four specimens with

confining pressures of 0, 5, 10, and 15 are numerically simulated. Because the tensile strength of brittle materials is not as much as the compressive strength, the modified Mohr–Coulomb criterion built-in RFPA<sup>3D</sup> is adopted as the strength criterion of unit destruction (Wu et al. 2020). During the loading process, gradually apply it to the predetermined confining pressure value, and then apply the axial displacement after the confining pressure of the system stabilizes. The initial displacement is 0.001 mm, the single-step increment is 0.001 mm, and the load until the sample is destroyed.

### Basic principles of RFPA<sup>3D</sup>

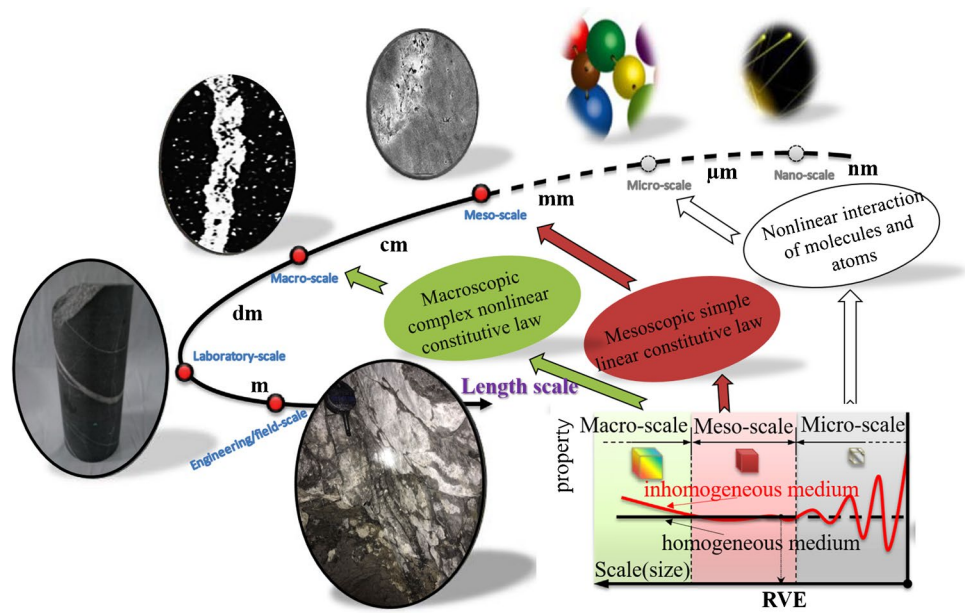
Multi-scale characteristics of defective sandstone in the study area and the relationship between different scales are shown in Fig. 4. Rock failure is a process of cross-scale nonlinear propagation and macro failure. RFPA<sup>3D</sup> can simulate the behavior of cross-scale continuum-discontinuity rocks. Considering the mesoscopic physical properties of various materials, the mesoscopic defects are summarized as RVE with uniform and simple mechanical properties at the mesoscopic level. Simply put, it is to build a bridge between microscopic structure and macroscopic through an intermediate scale (mesoscopic scale) (Li et al. 2014). The relationship between micro-evolution and macro-evolution is studied from the evolution process, and then the mechanical behavior of specimens is explained from the perspective of failure mechanism, which reduces the computational complexity.

The development of meso cracks determines the final macro failure mode. The place where cracks meet and penetrate is the area where the rock is further damaged. After the cracks are formed, the friction and extrusion between

**Fig. 3** Numerical model: **a** Internal slice of different parts; **b** distribution of internal joint; **c** distribution of pre-existing fracture



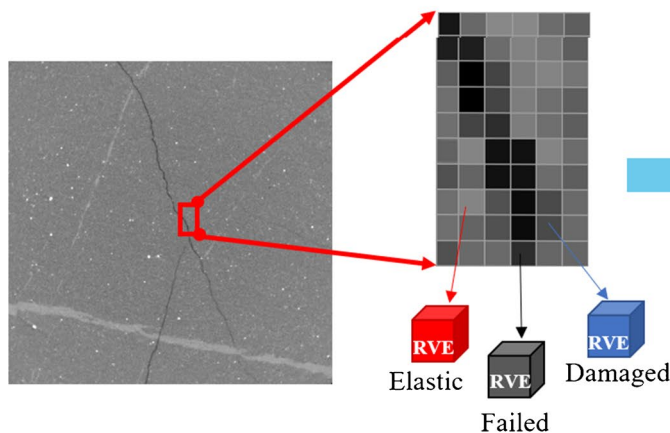
**Fig. 4** Relationship between different scale characteristics (Modify from Li et al. 2014)



the crack surfaces become the main damage of the rock. The fracture of sandstone is caused by the joint penetration and convergence of one or more groups of cracks, leading to the ultimate instability and failure of sandstone specimens. Figure 5 can be used to show the image transformation from macro crack pixels to grids in rocks. After enlarging the image, it can be seen the macro cracks consisting of many pixels with alike colors. Because the minimum crack width is equivalent to unit size, the more pixels per unit volume,

the closer the fine grid is to the mesoscale, and the closer the shown figure is to the real rock mass (Li et al. 2014). In RFPA<sup>3D</sup>, an RVE can only have one damage mode and correspond to one damage pattern, including elastic state, damage state, and failure state. Therefore, the direct element removal method can be used to describe the evolutionary process of RVE in the structure of elastic damage mechanics and reproduce the process of crack initiation, propagation, and penetration (Guo et al. 2021).

(a)



(b)

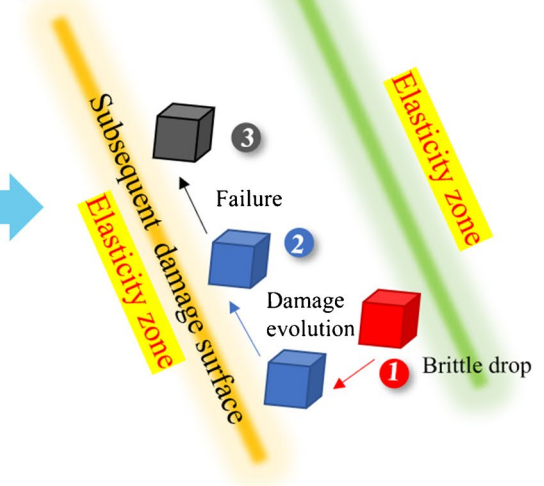


**Fig. 5** Evolution process of RVE

## Analysis

### Analysis of mechanical characteristics

The stress–strain curve of the specimen with confining pressure of 0 MPa can be apart for three stages (Fig. 6): In the elastic stage (A–C, where A is the starting point of the elastic stage, B is the midpoint of the elastic stage, and C is the endpoint of the elastic stage), the relation between stress and strain is analogously linearity, the slope is unchanged, and meso-fracture develops steadily; In the nonlinear deformation stage (C–E, D is the midpoint of the plastic stage, and E is the endpoint of the plastic stage), as the load spans about 70% of the peak strength, the slope of the curve decreases, indicating that the stress will continuously damage the specimen and reduce the strength. The stored elastic potential energy is released and irrecoverable plastic deformation occurs, and then some cracks are compacted. In the post-peak stage (E–G, F is the midpoint of the post-peak stage, and G is the endpoint of the post-peak stage), the stress dropped sharply, the internal meso-cracks spread through, resulting in macro-main cracks, the specimen was unstable and damaged, and the curve after the peak value nearly fell vertically, showing obvious brittle characteristics, and the bearing capacity gradually decreased but did not decrease to 0. The specimens still have the certain carrying capacity after rupture. As the stress reaches the peak point E, the crack does not completely penetrate the specimen, and if the load is applied continuously, new cracks and crack branching will continue to occur, so the occurrence time of the main crack and the maximum acoustic emission of the specimen lag behind the limit load.

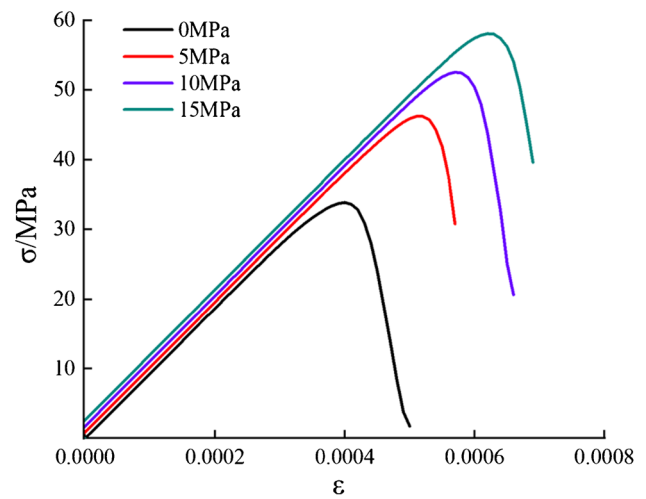
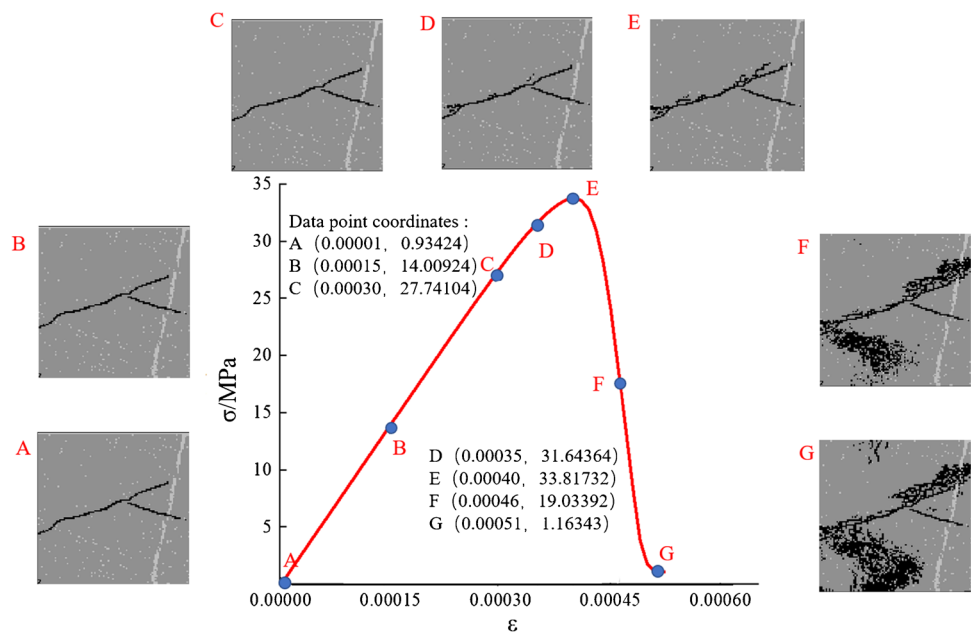
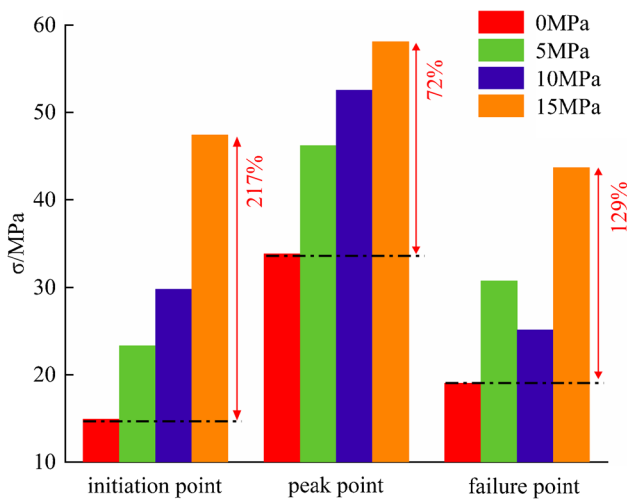


Fig. 7 Stress–strain curves

As shown in Fig. 7, the stress-strain of sandstone shows obvious anisotropy under the influence of confining pressure, but it still has the same mechanical action stage. As the displacement control quantity is used for loading, the initial quantity is 0.001 mm, and the curve is not the origin, so there is no obvious compaction stage for all specimens in the initial loading stage. The test piece is mainly subjected to elastic compression in the elastic stage, and the curve initially rises approximately in a straight line. Because the elastic modulus is the same when using RFP3D to assign sandstone particles, the simulated curve is approximately straight and parallel, and the greater the confining pressure, the greater the strain in the elastic stage. In the study scale range, the compressive strength of sandstone increases

Fig. 6 Full stress–strain curve and slice diagrams of specimen with confining pressure of 0 MPa





**Fig. 8** Stress changes of characteristic strength point

gradually with the increase of confining pressure. When the confining pressure is 0 MPa, the uniaxial compressive strength of the specimen is 33.82 MPa and the strength is the smallest, showing obvious brittle failure characteristics, and the peak strain corresponding to the peak stress is small. When the confining pressure is 15 MPa, the uniaxial compressive strength is 58.10 MPa and the strength is the maximum. This is because the increase of confining pressure makes the internal micro cracks of sandstone closed, and the ability to resist external force damage is enhanced. The greater the stiffness, the greater the stability of the local structure of the specimen, that is, the more difficult the sandstone is to deform. Macroscopically, it is shown that the sandstone specimen fails only under large strain. The later it reaches the peak point, the higher the sandstone strength, the weaker the brittleness and the stronger the ductility.

**Fig. 9** Fracture evolution diagram of the specimen with confining pressure of 0 MPa. **a** Numerical model fracture process; **b** Elastic modulus diagram; **c** Y-axis cutting diagram; **d** X-axis cutting diagram; **e** Corner cut diagram; **f** Acoustic emission evolution diagram; **g** Elemental damage diagram

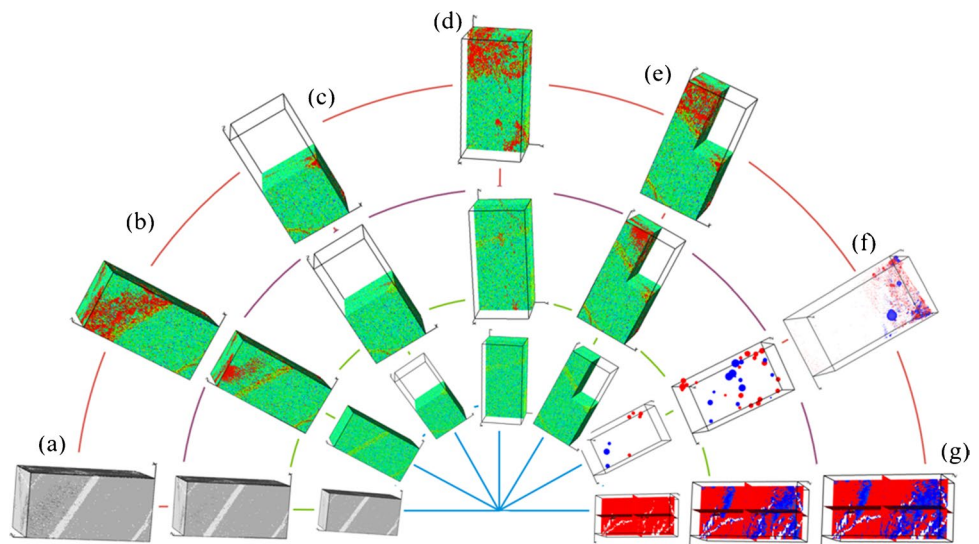


Figure 8 compares the stress at initiation point, peak point, and failure point of the specimen. At each characteristic strength point, the stress mostly increases with the rise of confining pressure. The stress distribution of the characteristic strength point of the specimen with confining pressure of 15 MPa is risen by 217%, 72%, and 129% as against the specimen with confining pressure of 0 MPa. This is because the specimen is not easy to deform under high confining pressure, and the crack initiation and penetration are lagging behind that of the specimen under low confining pressure.

Combined with engineering practice, as the rise of mining depth, the fracture mechanism of sandstone is also transformed, from the brittle property or fracture toughness-controlled failure in the shallow part to the fracture growth failure controlled by lateral stress in the deep mining condition, that is, from the dynamic brittle failure in the shallow part to the quasi-static ductile failure in the deep part (Li et al. 2014).

### Analysis of rupture characteristics

In the elastic stage, the mesostructure heterogeneity of the specimen leads to the crack of sandstone in the upper-middle position. In the nonlinear deformation stage, the crack extends to the maximum compressive stress along the weak plane in a curve form, forming a fracture surface with many small branches. With the loading proceeding, the crack rapidly propagates along the weak structural plane at the lower end. And the number and length of cracks keep increasing until the through instability (Fig. 9a and b). In Fig. 9c, the Z-axis cutting diagram contains two crack propagation modes, which are more complicated due to the existence of original defects such as joints and cracks. From Fig. 9d, X-axis cutting diagram, with the growth of axial load, the

cracks spread along the weak structural plane to both ends, eventually forming many secondary cracks. These cracks are parallel to the loading direction. Although they do not penetrate through the whole specimen, they mesh and overlap each other in space. In the schematic diagram of corner-cutting of Fig. 9e, we can see the internal defects of the specimen, the characteristics of the meso-spatial structure, and the cracking of various sections.

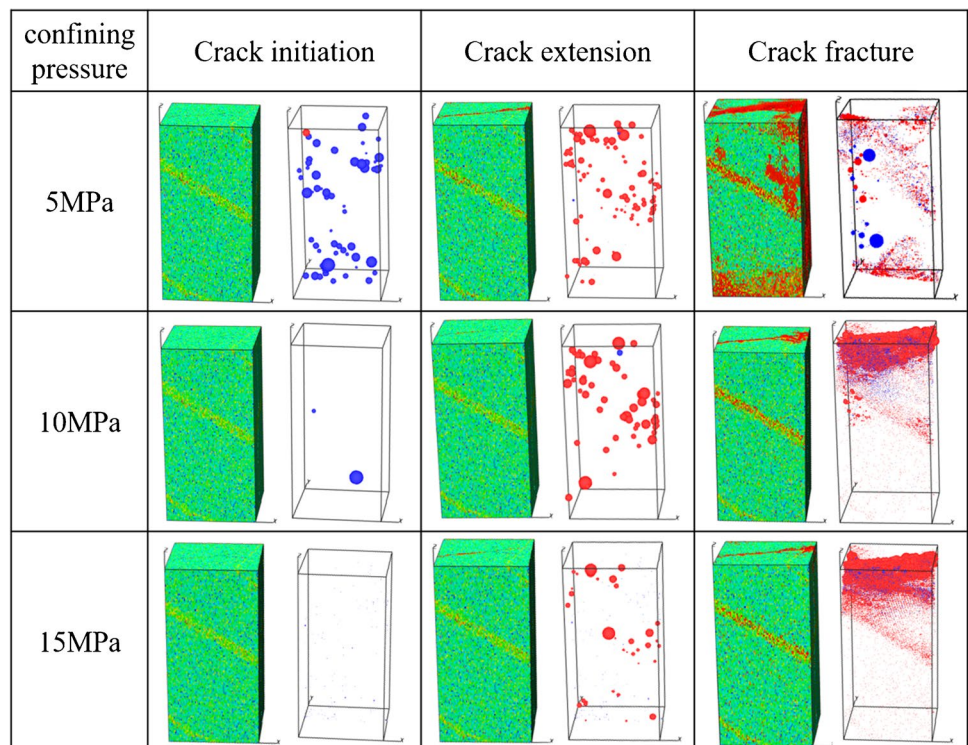
In Fig. 9f, acoustic emission evolution diagram, each ball represents an acoustic emission. The larger the ball diameter, the greater the acoustic emission energy release in this step. The center of the ball is the position of the failed unit, blue represents tensile failure, and red represents shear failure (Lang et al. 2019). In the elastic stage, there is tensile stress concentration in a small range at the end of the joint, and compressive stress concentration in the original crack, which is characterized by scattered micro-point source fracture. It shows that the original defect position is fragile and easy to damage. As the loading progresses, the energy gradually gathers into pieces, and when it accumulates to a certain extent, many large blue acoustic emission balls will appear in the specimen, which indicates that macroscopic crack is tensile failure. Most of the energy released by the specimen in the process of fracture comes from the fracture zone in the high-stress area, and the shear failure is the main failure close to the interface between the specimen and the load board. The tensile failure of the meso-unit causes the initiation and expansion of mesopores and cracks of sandstone, which is because sandstone can withstand compression but

not tension, and the tensile stress first reaches the tensile strength when confining pressure is 0 MPa.

Figure 9g is the damage diagram of the unit in the loading process of the specimen, in which the blue color represents the damaged unit. In the elastic stage, the isotropic stress has little influence on the specimen, and almost no major damage. In the nonlinear deformation stage, meso-damage began to occur in the two different particle cementation places of calcite vein and sandstone matrix, and the number of internal damage units continued to increase. Part of the damaged element becomes the initial position of the surface crack. In the post-peak stage, the damage units around the original defects are very dense and deep, and the damage between different particles is connected. When the number of meso-damage points through the connection reaches a certain degree range, it will cause irreversible macro-damage. The original defect is the most vulnerable part, the damage of the elements at the junction and joint of cracks is the most serious. The order of damage evolution of the specimen is that it spreads from inside to outside and finally extends to the surface of the specimen.

A series of fracture zones caused by shear failure is formed at the contact under confining pressure, and the fracture zones extend beyond the local deformation zone along the loading direction (Fig. 10). Under the control of tensile stress, the inclined single-wing tensile cracks along the joint direction began to occur in the specimen and spread along the weak plane, and the direction of expansion is approximately parallel to the maximum principal stress direction.

**Fig. 10** Fracture process and acoustic emission evolution of specimens





As the loading progresses, the specimen forms a macroscopic shear band. When the loading time is long, the initial crack can fully expand, and failure is mainly controlled by several large cracks, and several secondary cracks overlap and penetrate each other to form a macro rupture surface, which leads to the instability. Under the influence of confining pressure, the shear rupture along the joint surface and the tensile rupture through the joint surface occurred. Among them, the specimen with confining pressure of 5 MPa is the mixed tension-shear rupture, yet the specimens with confining pressure of 10 MPa and 15 MPa are subjected to shear failure.

The influence of confining pressure is discussed by comparing the displacement nephogram and stress nephogram of specimens with confining pressure of 0 MPa and 15 MPa shown in Fig. 11. According to the analysis of the Z-displacement nephogram sequence, it can be seen that the deformation field of sandstone deformation and failure process is non-uniform evolution, and there are obvious zoning phenomena. With the loading, the location and area

of the deformation field division will change continuously. The zoning evolution of the deformation field mainly goes through three stages. In the beginning, the high displacement is concentrated in the lower part, the upper part is a low displacement, and the transition zone is bounded by the boundary between them, which changes with it. In the elastic stage, the high displacement zone with confining pressure of 0 MPa decreases, and the area of low displacement zone increases, while the displacement of the specimen with confining pressure of 15 MPa changes inversely. In the post-peak stage, the zoning of the displacement field was redistributed. The specimen with confining pressure of 0 MPa formed obvious displacement zoning along the joint direction. While the specimen with confining pressure of 15 MPa had no obvious displacement zoning, the areas and positions of the high displacement zone, the low displacement zone, and the intermediate transition zone are unchanged.

The diagram of maximum principal stress displays the principal stress distribution of sandstone, and there is a remarkable evolution law of stress field during loading.

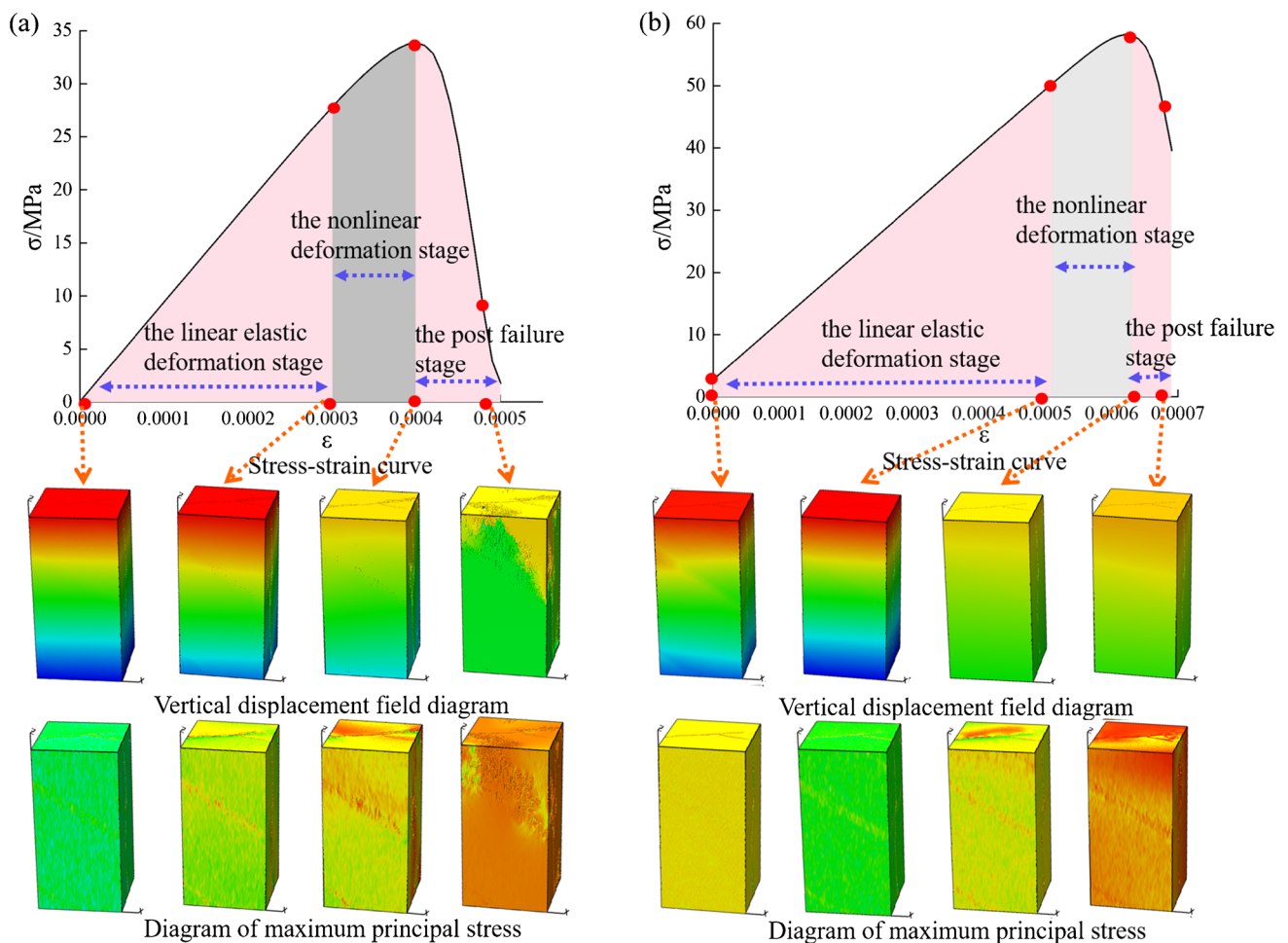


**Fig. 11** Evolution nephogram of surface stress field and displacement field: **a** confining pressure is 0 MPa specimen; **b** confining pressure is 15 MPa specimen

The internal stress distribution is inhomogeneous, and it produces uneven stress localization zones in their respective principal stress fields, especially the critical interface between joints and sandstone has obvious stress concentration (Red indicates that the stress is relatively low, green indicates that the stress is relatively high. It transits in the order of red, yellow, green, and blue, which means that the numerical value gradually increases). It is because the stress concentration at the junction of the two materials belongs to the unstable area, which is prone to crack. The localized zone loaded with stress on the eve of failure is often the potential fracture location of specimen failure. As the loading progresses, the specimen gradually reaches a new stress balance. The localized zone disappears, and new and regular high-stress zones appear. Under high confining pressure, the stress concentration is not obvious, and there is no obvious crack on the surface of the specimen, but there is a certain meso crack inside; confining pressure limits the crack propagation and growth.

### Analysis of fractal feature

Two-dimensional fractal dimension is defined as

$$D_2 = \lim_{k \rightarrow \infty} \frac{\lg N r_k(A)}{\lg \frac{1}{r_k}} \quad (2)$$

Among them,  $D_2$  is the fractal dimension;  $r_k$  is the developed reducing sequence with element's square box size;  $N_{r_k}(A)$  is the least number of meshes needed for covering the target set  $A$  with a square box of size  $r_k$  (Liu et al. 2021).

The specimen with confining pressure of 0 MPa is taken as an example; the distribution of cracks cannot be seen intuitively because of the low resolution of the picture and high artifacts. On the premise of retaining the distribution characteristics of fractures in sandstone, the slice is binarized to obtain the picture as shown in Fig. 12. Then, import it into the self-compiled MATLAB box dimension calculation program to operate. The fitting curve of fractal characteristics in Fig. 13 shows that the correlation coefficient  $R^2$  is 0.9754, and the fractal dimension  $D_2$  is 1.1595, which shows

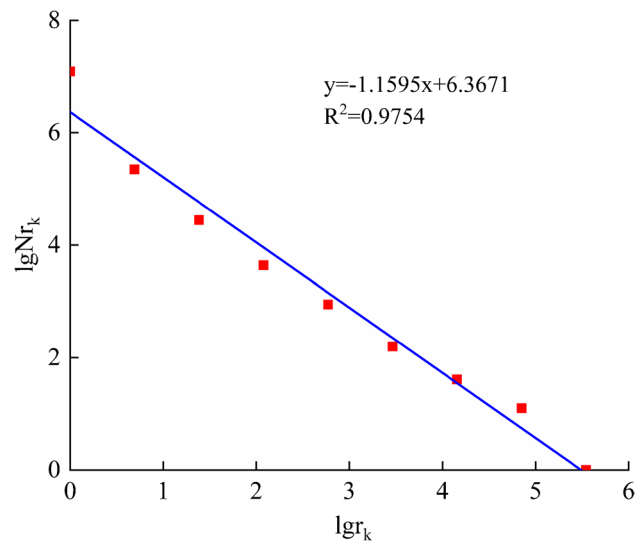


Fig. 13  $\sigma=0\% \sigma_{max}$ , the fitting curve of two-dimensional fractal characteristics of specimen with confining pressure of 0 Mpa

that the mesoscopic scale fracture distribution of sandstone has good self-similarity (points A–F correspond to different stress stages in Fig. 6, the same below).

Two-dimensional scanning images can only reflect the local information of fractures, while three-dimensional structures can completely and intuitively show the spatial distribution of cracks; it offers a basis for the accurate evaluation of the overall crack structure. Three-dimensional fractal dimension is defined as

$$D_3 = -\lim_{s \rightarrow 0} \frac{\lg N(s)}{\lg(s)} = \lim_{s \rightarrow 0} \frac{\lg N(s)}{\lg(1/s)} \quad (3)$$

Among them,  $D_3$  is the fractal dimension,  $s$  is the edge length of cube, and  $N(s)$  is the minimum number of cubes covering the point set  $F$ .

To identify the shape and distribution of cracks in the image, based on the principle of 3D reconstruction, RFPA<sup>3D</sup> post-processing slice cracks are extracted by a self-made command stream to obtain the coordinates of crack pixel scale points, and then, the three-dimensional crack distribution diagram is obtained (Fig. 14). Import it into the

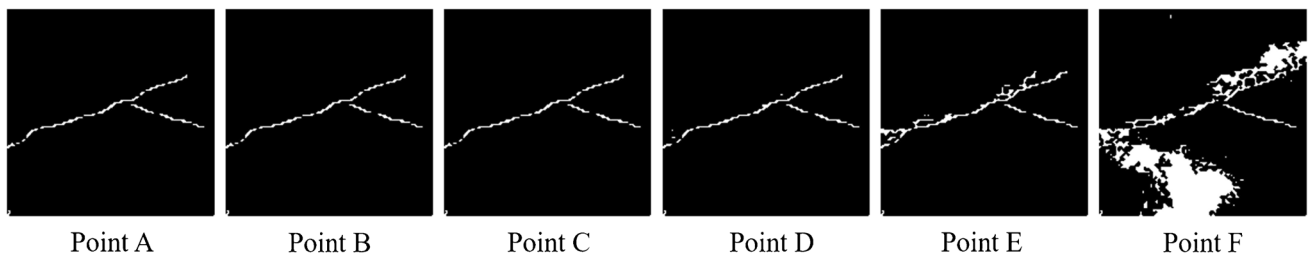
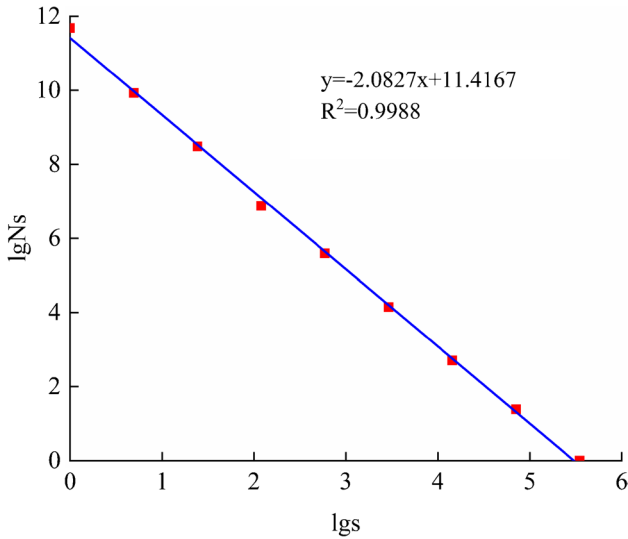
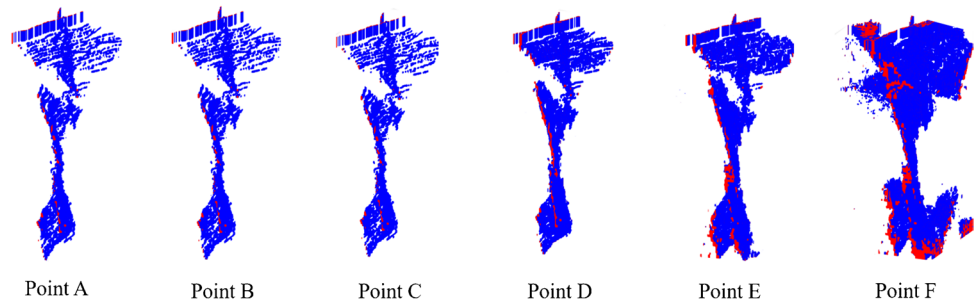


Fig. 12 Two-dimensional crack distribution diagram of the specimen with confining pressure of 0 MPa under different stress levels

**Fig. 14** Three-dimensional crack distribution diagram of the specimen with confining pressure of 0 MPa under different stress levels



**Fig. 15**  $\sigma=0\%\sigma_{max}$ , the fitting curve of three-dimensional fractal characteristics of the specimen with confining pressure of 0 Mpa

self-made box dimension calculation program to get the fractal characteristic fitting curve of Fig. 15. The calculated  $D$  is 2.0827, and the correlation coefficient  $R^2$  is 0.9988, which shows that the  $D$  is highly reliable.

See Fig. 16 for the  $D$  of the specimen under different stress levels. With the rise of stress level, the internal damage of the specimens accumulates, and the  $D$  increases. In the elastic stage, the  $D$  of the specimens is unchanged, and no major damage has occurred. In the nonlinear deformation stage, the  $D$  increases slightly. In the post-peak stage, the more complex the shape of the spatial network,  $D$  shows a linear increasing trend, which indicates that the crack expansion and evolution in the process of rock fracture mainly take place during this stage. The  $D$  of cracks of the specimen corresponds to each stress stage in the process of sandstone failure, which can describe the process of fracture and weakening of rock during loading.

The fracture difference of specimens under different confining pressures results in the difference of fractal dimension (Chen et al. 2001). As the increase of confining pressure, the  $D$  of sandstone specimens slowly decreases. As the confining

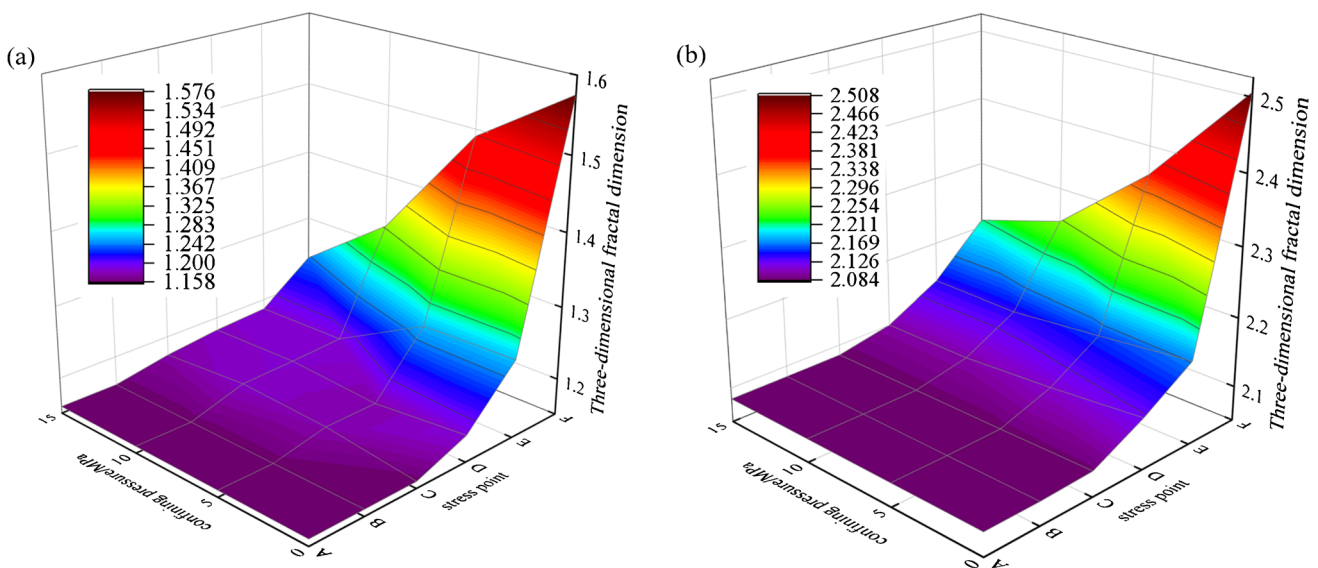


**Fig. 16** Fractal dimension of the specimens: **a** two-dimensional fractal dimension; **b** three-dimensional fractal dimension)

pressure is 0 MPa, the ultimate fracture mode is the most complex, the damage is the greatest, and the  $D$  is the largest (in which  $D_2$  is 1.5759, and  $D_3$  is 2.5065). As the confining pressure is 15 MPa, the fracture mode is the simplest, and the damage is the lightest. Therefore, the fractal dimension is the smallest (in which  $D_2$  is 1.2388 and  $D_3$  is 2.2106); The  $D$  of specimens with confining pressure of 5 MPa and 10 MPa is between them. This is because the size of the fractal dimension is primarily determined by the complexity of the fracture network. The higher confining pressure, the more difficult it is to nucleate, expand, and penetrate meso-cracks in rock, and the smaller the internal damage fracture surface, that is, the weaker the damage degree, the fractal dimension decreases, the rise of confining pressure further inhibits the development of internal fractures in sandstone. Therefore, the smaller the confining pressure, the worse the integrity, the more developed the cracks, the more complicated the fracture mode, the more serious the final crushing degree, the better the damaging effect, and the greater the fractal dimension.

Comparing the two-dimensional and three-dimensional fractal dimensions, we can see that the  $D_2$  ranges from 1.1595 to 1.5759, and the  $D_3$  ranges from 2.0827 to 2.5065. The two fractal dimensions respectively reflect the failure degree of sandstone specimens from the local and overall development degree and fracture degree of cracks; it can quantitatively evaluate the spatial distribution, development, and evolution process of internal cracks at the mesoscopic scale. Although the variation trend of the two fractal dimensions with confining pressure is consistent, compared with the two-dimensional fractal dimension, the change rate of fractal dimension of the three-dimensional fracture image before peak stress is smaller, and there is almost no obvious change before the nonlinear deformation stage. This is because the two-dimensional fractal dimension mainly reflects the evolution of the fracture network of sandstone section under load, but sandstone is a heterogeneous porous geological material, and the distribution of internal pores and fractures is anisotropic. The changing trend of each section is different, and the three-dimensional fractal dimension makes up for the deficiency of the two-dimensional fractal dimension and effectively describes the evolution law of the overall fracture network of the loaded sandstone from the perspective of three-dimensional.

## Conclusion

1. Confining pressure has an important role to mechanical properties. The compressive strength, cracking strength, and failure strength are anisotropic as a result of this influence. Affected by different confining pressures,

there is a time and position difference in the internal energy accumulation of sandstone.

2. The cumulative development of microfracture is in harmony with the macro rupture mode. Damage evolution of the specimen is that it spreads from inside to outside and finally extends to the surface of the specimen. The 0 MPa specimen is a tensile failure, the 5 MPa specimen is a tensile-shear mixed failure, and the 10 MPa and 15 MPa specimens are shear failures.
3. The material damage evolution process is fractal, and the fractal dimension is the primary parameter to mirror the degree of material damage. As the confining pressure is 0 MPa, the fractal dimension is the largest, the crack propagation is the fullest, the rupture mode is the most complex, and the damaging effect is relatively good. The damage is restrained as confining pressure rises, and the fractal dimension of the fracture drops. There is a high correlation between fractal dimension and confining pressure.
4. The initiation, expansion, and penetration of cracks in loaded sandstone specimens follow the crack variation law in two-dimensional sections. However, when compared to the two-dimensional fracture structure, the dynamic evolutionary process of three-dimensional structure more intuitively and accurately reflects internal fracture shape and distribution of specimens during deformation and failure.
5. Stress distribution, crack propagation path, failure mode, and macroscopic fracture process are all affected by meso-heterogeneity and the presence of original defects. Sandstone materials have obvious non-uniformity and statistical characteristics of strength, which means that the original defects, such as joints and other low-strength areas, destruction first, followed by the high-strength areas.

**Funding** Financial support provided by the National Natural Science Foundation of China (No. 51774101 and No. 51964007), the Guizhou Mining Power Disaster Early Warning and Control Technology Innovation Team, China (No. 2019–5619), the Startup Project for High-level Talents Training Project in Guizhou Province, China (No. 2016–4011), and the Guizhou Science and Technology Department (Grant Number [2021]general 516).

## Declarations

**Conflict of interest** The authors declare no competing interests.

## References

- Chen P, Wang EY, Ou JC et al (2013) Fractal characteristics of surface crack evolution in the process of gas containing coal extrusion. *Int J Min Sci Technol* 23(1):121–126. <https://doi.org/10.1016/j.ijmst.2013.03.001>



- Chen QG, Zuo YJ, Lin JY et al (2022) Numerical research on response characteristics of surrounding rock for deep layered clastic rock roadway under static and dynamic loading conditions. *Geomech Geophys Geo-Energy Geo-Resour* 8:91. <https://doi.org/10.1007/s40948-021-00329-3>
- Chen ZH, Tan GH, Yang WZ (2001) Numerical simulation of damage and failure of rocks under different confining pressures. *Chin J Geotech Eng* 5:576–580
- Cnudde V, Masschaele B, Dierick M et al (2006) Recent progress in X-ray CT as a geosciences tool. *Appl Geochem* 21(5):826–832
- Guo P, Yuan Y, Peng Y et al (2021) Analysis of slope stability and disaster law under heavy rainfall. *Geofluids* 3:1–17. <https://doi.org/10.1155/2021/5520686>
- Hao ZB, Zuo YJ, Liu H et al (2022) Mesoscopic damage evolution characteristics of jointed sandstone under different loading conditions. *Geomech Geophys Geo-Energy Geo-Resour* 8:92. <https://doi.org/10.1007/s40948-022-00390-6>
- Hou P, Ju Y, Gao F et al (2016) Simulation and visualization of the displacement between CO<sub>2</sub> and formation fluids at pore-scale levels and its application to the recovery of shale gas. *Int J Coal Sci Technol* 3(4):351–369. <https://doi.org/10.1007/s40789-016-0155-9>
- Lang YX, Liang ZZ, Dong Z (2019) Reconstruction of 3D meso-pore model of basalt and numerical experiment of direct tension. *Chinese J Eng Sci* 41(08):997–1006. <https://doi.org/10.13374/j.issn.2095-9389.2019.08.005>
- Li SG, Zhang JH, Cheng LH et al (2014) Numerical simulation study of easy-weathering roadway support in deep soft rock strata. *Min Saf Environ Prot* 41(02):1–4+8. <https://doi.org/10.3969/j.issn.1008-4495.2014.02.001>
- Liu H, Zheng LL, Zuo YJ et al (2021) Study on mesoscopic damage evolution characteristics of single joint sandstone based on micro-CT Image and fractal theory. *Shock Vib* 2021:1–18
- Liu ZQ, Zheng LL, Liu H et al (2022) Fractal analysis of failure process and damage evolution of jointed sandstone based on DIP technique. *Math Probl Eng* 2022:1–14. <https://doi.org/10.1155/2022/7528535>
- Mandelbrot BB (1998) The fractal geometry of nature [J]. *Am J Phys* 51(3):468
- Mao LT, Xue R, An LQ et al (2005) Fractal approach on soft soil porosity microstructure. *J China Univ Min Technol* 34(5):600–604. <https://doi.org/10.3321/j.issn:1000-1964.2005.05.012>
- Masri M, Sibai M, Shao JF et al (2014) Experimental investigation of the effect of temperature on the mechanical behavior of Tournemire shale. *Int J Rock Mech Min Sci* 70(Complete):185–191. <https://doi.org/10.1016/j.ijrmms.2014.05.007>
- Singh M, Samadhiya NK, Kumar A et al (2015) A nonlinear criterion for triaxial strength of inherently anisotropic rocks. *Rock Mech Rock Eng* 48:1387–1405. <https://doi.org/10.1007/s00603-015-0708-z>
- Song H, Wu Z, Wang A et al (2020) Study on the microscale tensile properties of lower Cambrian Niutitang Formation shale based on digital images. *Geofluids* 5:1–14. <https://doi.org/10.1155/2020/8828965>
- Tang M, Wu Z, Wang A et al (2021) Study on the microscopic fracture process and acoustic emission of shale based on digital image. *Geofluids* 8:1–14. <https://doi.org/10.1155/2021/8874918>
- Wang G, Yang XX, Zhang XQ et al (2016) Numerical simulation on non-Darcy seepage of CBM using 3D reconstruction based on computed tomography. *J China Coal Soc* 41(4):931–940. <https://doi.org/10.13225/j.cnki.jccs.2015.0849>
- Wang DK, Zhang P, Wei JP et al (2019) Research on the dynamic evolution of 3D fracture structure of loaded coal body based on CT visualization. *J China Coal Soc* 44(2):574–584. <https://doi.org/10.13225/j.cnki.jccs.2019.0647>
- Wang Y, Wen Z, Liu G et al (2020) Explosion propagation and characteristics of rock damage in decoupled charge blasting based on computed tomography scanning. *Int J Rock Mech Min Sci* 136(3):104540. <https://doi.org/10.1016/j.ijrmms.2020.104540>
- Weibull W (1951) A statistical distribution function of wide applicability. *J Appl Mech* 18:293–297. <https://doi.org/10.1093/qjmmam/6.4.453>
- Wu Z, Zuo Y, Wang S et al (2016) Numerical simulation and fractal analysis of mesoscopic scale failure in shale using digital images. *J Petrol Sci Eng* 145:592–599. <https://doi.org/10.1016/j.petrol.2016.06.036>
- Wu YN, Zhang Z, Wang XZ et al (2021) Study on the physical properties and joint evolution characteristics of three-dimensional reconstructed coal. *Adv Mater Sci Eng*. <https://doi.org/10.1155/2021/7038110>
- Wu Z, Lou Y, Yin S et al (2020) Acoustic and fractal analyses of the mechanical properties and fracture modes of bedding-containing shale under different seepage pressures. *Energy Sci Eng* 8(10). <https://doi.org/10.1002/ese3.772>
- Wu H (2017) Research on dominant grouping and dynamic modeling method of a rock fracture network in the dam foundation of hydro-power project. Tianjin University
- Xie HP (1996) An introduction to fractal - rock mechanics. Science Press, Beijing
- Yang SQ, Jiang YZ, Xu WY et al (2008) Experimental investigation on strength and failure behavior of pre-cracked marble under conventional triaxial compression. *Int J Solids Struct* 45(17):4796–4819. <https://doi.org/10.1016/j.ijsolstr.2008.04.023>
- Yang SQ, Jing HW, Wang SY (2012) Experimental investigation on the strength, deformability, failure behavior and acoustic emission locations of red sandstone under triaxial compression. *Rock Mech Rock Eng* 45(4):583–606. <https://doi.org/10.1007/s00603-011-0208-8>
- Yi SM, Zhao WQ (1990) The fractal characteristics of the three gorges dam foundation rock under the conditions of uniaxial compression. *Chin J Rock Mech Eng* 18(5):520–523
- Yue ZQ (2006) Digital representation of meso-geomaterial spatial distribution and associated numerical analysis of geomechanics: methods, applications and developments. *Chin J Rock Mech Eng* 25(5):875–888. <https://doi.org/10.3321/j.issn:1000-6915.2006.05.002>
- Zhao YX, Liu SM, Zhao GF et al (2015) Failure mechanisms in coal: dependence on strain rate and microstructure. *J Geophys Res: Solid Earth* 119(9):6924–6935. <https://doi.org/10.1002/2014JB011198>

Springer Nature or its licensor (e.g. a society or other partner) holds exclusive rights to this article under a publishing agreement with the author(s) or other rightsholder(s); author self-archiving of the accepted manuscript version of this article is solely governed by the terms of such publishing agreement and applicable law.